In Situ Double Anomalous Small-Angle X-ray Scattering of the Sintering and Calcination of Sol−Gel Prepared Yttria-Stabilized-Zirconia Ceramics

Twilight Barnardo,* Kristin Hoydalsvik, and Rudolf Winter

Materials Physics, Aberystwyth University, Penglais, Aberystwyth SY23 3BZ, Wales

Chris M. Martin and Graham F. Clark

Synchrotron Radiation Source, STFC Daresbury Laboratory, Warringtom WA4 4AD, England

Received: February 10, 2009; Revised Manuscript Received: April 21, 2009

Yttria-stabilized-zirconia xerogels are heat treated to temperatures of 1000 °C, and the evolving structures are analyzed using anomalous small-angle X-ray scattering (ASAXS) across two absorption edges. Homogeneous nanocrystals (∼10 nm in size) begin to grow at temperatures above 390 °C for pure YSZ, while the presence of a silica matrix inhibits nucleation until 780 °C. Anomalous effects have shown that zirconia plays the dominant role in crystal growth and that varying concentrations of yttria do not affect the nucleation temperatures or average size of the individual particles. The difference between scattering factors, necessary for accurate ASAXS analysis, is also investigated. Relations for this analysis were derived from X-ray absorption spectra, conducted as part of the small-angle scattering investigations.

Introduction

Yttria-stabilized zirconia (YSZ) has wide use in solid-state electrolyte applications such as oxygen sensors and solid fuel cells.[1] Though the parent lattice, zirconia, is usually found in the monoclinic state in ambient conditions, high temperatures can alter the crystalline phases to be tetragonal (1400 °C) and cubic (2400 °C), respectively. The presence of rare-earth or alkaline-earth ions can force the zirconia to stabilize in either the tetragonal or cubic phase at a much lower temperature.[1] A thermally activated conduction process is thus achieved through formation of oxygen vacancies within the stabilized zirconia lattice.[2]

In a typical synthesis, YSZ is produced by the coprecipitation method.[3] Industrial scale production by the comilling technique[4] and, more recently, microwave flash have also been suggested.[5] The sol−gel method offers the additional opportunity to produce a wider range of YSZ-based glasses and ceramics, as well as dip coated substrates and YSZ ceramic fibers.

Traditional sol−gel methods involve the hydrolysis of alkoxide precursor materials under controlled conditions.[6] Transition metal alkoxides, however, are generally quite reactive and require the addition of a chelating agent such as acetylacetone to assist in gel formation.[7] To produce a clear, homogeneous YSZ gel, acetylacetone is added such that its molar ratio to metal ions is equal to one, and gelation can thus be induced by careful injection of a water−alcohol solution at 50 °C. The resultant gels can be dried in air (xerogels), or solvents can be extracted by supercritical drying with carbon dioxide (aerogels), depending on the desired properties of the final product.[8]

Small-angle X-ray scattering (SAXS) is a method widely used in the analysis of internal nanoscale structures. The technique is extremely useful in determining the size and shape of particles, as well as how they interact. In general terms, a scattering intensity at small angles can be defined as equal to

$$I(q) = N r_e^2 \Delta\rho^2 V^2 |F(q)|^2 S(q) \quad (1)$$

where N is the particle number density, $\Delta\rho$ is the difference in electron density between the primary particles and the surrounding matrix or air, r_e is the classical electron radius, V is the average particle volume, $F(q)$ is the particle form factor (shape), $S(q)$ is the structure factor, and q is the momentum transfer with units of inverse length (r), and is given by

$$q = \frac{4\pi \sin(\theta)}{\lambda} \quad (2)$$

This relation can give useful information on the shape (form) of the particles and their overall surface roughness. For smooth surfaces such as spheres, the particle form factor is given by

$$F(q) = 3\left(\frac{\sin(qr) - qr\cos(qr)}{q^3 r^3}\right) \quad (3)$$

From eq 1, $I(q)$ is proportional to the square of the form factor. In the limits $qr \rightarrow 2\pi$, inserting $F(q)$ into eq 1 gives the Porod relation for smooth surfaces[9] (eq 4). The Porod approximation is valid for large q, i.e., when $qr \gg 1$.

$$I(q) \propto q^{-4} \quad (4)$$

Gels are composed of agglomerations of small primary particles ($r_p \sim 0.3$ nm for silica and 1.2 nm for zirconia) of fractal dimension d. This allows us to define an adjustment to eq 4 to use the Porod scheme as a measure of surface roughness. For such materials, the number of particles is instead proportional to q^d at high q,[9] so eq 4 becomes

$$I(q) \propto q^{-\alpha} \quad (5)$$

The exponent α is given by $\alpha = 6 - d$. Surface roughness can thus be measured by taking the gradient of log intensity versus log q.

Modern synchrotron radiation sources offer beams of high intensity, meaning scattering patterns can be obtained in seconds,

* To whom correspondence should be addressed. E-mail: twi@ishatar.com.

10.1021/jp9012202 CCC: $40.75
Published on Web 05/15/2009

and good time-resolved scattering data can be achieved which will track nanometer scale changes in situ.[10,11]

SAXS is performed at a single fixed energy. This poses a disadvantage as the resultant scattered photons do not present any chemical information on individual species within composite materials. However, when the X-ray energies close to the absorption edge of a given element are tuned, the material's overall scattering function will change. Anomalous scattering presents the opportunity to utilize the changes a scattering pattern exhibits close to an absorption edge.[12,13,17] This natural phenomenon can be used to resolve the patterns one would obtain from different species within the sample.

Previous work in anomalous small-angle scattering in situ has included the measurement of scattering functions below and above the absorption edge and subtraction of them to obtain the scattering contribution of the parent element.[13] There has even been some work on comparing scattering functions from successive measurements at beam energies close to the edge ex situ.[14]

A much more detailed analysis is obtained when one generates a succession of scattering patterns very close to the absorption edge (to 1 or 2 eV), with an additional measurement far below. The resultant scattering functions can be reduced by solving a system of simultaneous equations (eq 6), which contain the resonant correction to the atomic scattering factors, producing three new scattering functions dependent on species.[12,15]

$$I(q) = f_0^2 I_n(q) + 2f_0 f' I_c(q) + (f'^2 + f''^2) I_r(q) \quad (6)$$

While the normal (first) term is equivalent to a SAXS pattern taken far below any absorption edge, it is the cross and resonant terms that provide the additional chemical information. The cross (middle) term describes how the ions interact with the remaining sample, and this can be negative. A resonant contribution provides information on like scatterers; the function one would obtain without the presence of the matrix. To date, only a few static ex situ experiments have been performed using this technique.[12,16,17]

Determining the Resonant Correction to the Atomic Scattering Factors

One of the most fundamental requirements for good anomalous small-angle X-ray scattering (ASAXS) deconvolution is accurate determination of the atomic scattering factors. Previous ASAXS studies have used resonant corrections determined from theoretical calculations.[18] However, these values are calculated for pure elements only and do not take into account other materials, such as mixed oxides, where other elements are present.

Corrections to the atomic scattering factors are determined by means of the Kramers−Kronig transforms (eq 7) which give two values, f' and f'', as a function of energy. Values for f'' are determined by the measurement of the absorption spectrum (EXAFS).

$$f'(E) = \frac{2}{\pi} \int_0^\infty \frac{E f''(E)\, dE}{E_0^2 - E^2} \quad (7)$$

Figure 1 shows a comparison between theoretical values and those determined from yttria-stabilized zirconia, which were derived from X-ray absorption spectra. One can clearly see the presence of the yttrium and zirconium absorption edges in the sample, which have a drastic effect on the atomic scattering factor corrections. The presence of the fine structure wiggles (unique to the compound) generates additional features just

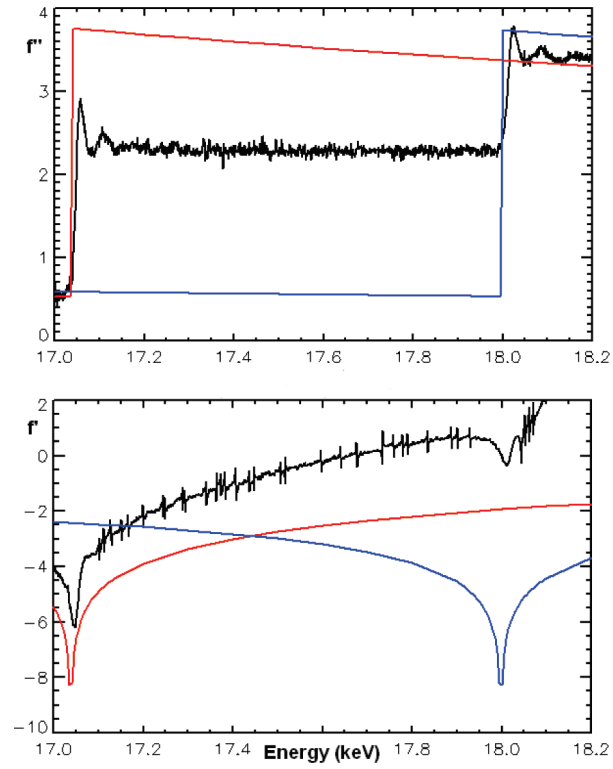

Figure 1. Comparison between theoretically and experimentally derived values for the resonant corrections to the atomic scattering factors as a function of energy (in keV), f'' (top) and f' (bottom). The two smooth curves in each panel represent the theoretical curves for yttrium (step/minimum near 17 keV) and for zirconium (feature near 18 keV). The two curves are weighted by the Y/Zr molar ratio to derive a theoretical curve for a given composition. An experimental curve for a sample with a molar ratio of 50 mol %, showing features at both energies, is superimposed for comparison.

above the edges which are ignored in the f' and f'' tables.[18] An additional factor is the narrowing of the width of the minimum in f'; this limits the range of energies that can be used for good ASAXS contrast to several electronvolts. The relative sizes of the steps (in f'') and minima (in f') are also dependent on the concentration of the species. A sample with a higher concentration of yttrium will have a different scattering factor from YSZ with little yttrium present.

The ratio of the step sizes depends linearly on the Y/Zr ratio with both edges being equal in intensity when the yttria concentration is 33 mol %. This is due to yttria primary particles existing in the Y_2O_3 state, while zirconia is in the form ZrO_2. Using this linear relation, the corrections to the atomic scattering factors across the yttrium edge can be calculated for a wide range of YSZ samples. The presence of a silica matrix does not affect the relative step sizes for given yttria concentrations.

Anomalous scattering data is reduced by the matrix form of eq 6. In single ASAXS, this is a series of simultaneous equations for each value of q (eq 8), where I_{E_1}, I_{E_2}, and I_{E_3} are the scattering functions obtained from three different X-ray energies.

$$\begin{pmatrix} f_0^2 & 2f_0 f'_{E_1} & f'^2_{E_1} + f''^2_{E_1} \\ f_0^2 & 2f_0 f'_{E_2} & f'^2_{E_2} + f''^2_{E_2} \\ f_0^2 & 2f_0 f'_{E_3} & f'^2_{E_3} + f''^2_{E_3} \end{pmatrix} \begin{pmatrix} I_n \\ I_c \\ I_r \end{pmatrix} = \begin{pmatrix} I_{E_1} \\ I_{E_2} \\ I_{E_3} \end{pmatrix} \quad (8)$$

For multiple ASAXS, the scattering corrections for each additional absorption edge need to be included, along with their appropriate normal, cross, and resonant terms, to give the general case (eq 9).

$$\begin{pmatrix} A_1 & 0 & \dots & 0 \\ 0 & A_2 & \dots & 0 \\ \dots & \dots & \dots & \dots \\ 0 & 0 & \dots & A_n \end{pmatrix} \begin{pmatrix} X_1 \\ X_2 \\ \dots \\ X_n \end{pmatrix} = \begin{pmatrix} B_1 \\ B_2 \\ \dots \\ B_n \end{pmatrix} \quad (9)$$

Here, A are three by three matrices containing the resonant corrections, and X and B are column vectors containing the normal, cross, and resonant terms and the scattering functions from three energies for each species, respectively. In double ASAXS, eq 9 is reduced to a diagonal six by six matrix.

Experimental Method

Yttrium isopropoxide solution was prepared by dissolving 1.5 g of anhydrous yttrium(III) chloride in 25 mL of isopropanol (IPA) in a dry nitrogen atmosphere. An additional 25 mL of isopropanol was reacted with 1.46 g of clean potassium metal. The resultant two solutions were then mixed and vigorously stirred under reflux at 80 °C for 3 h to produce a clear solution of yttrium isopropoxide and a potassium chloride precipitate which was removed by centrifugation.[19]

As shown in Table 1, sol−gel samples were produced by mixing 12 mL of zirconium *n*-propoxide with 6 mL of isopropanol, 0.1 mL of acetic acid, and 2.25 mL of acetylacetone (AcAc), as a chelating agent, together with a selected quantity of yttrium isopropoxide solution. Gelation was induced by the introduction of 3 mL of isopropanol mixed with 2 mL of distilled water. The resultant sols were kept at 50 °C to produce clear, yellow, homogeneous gels after several hours.

A second batch of samples was prepared by adding 4 mL of tetraethylorthosilicate (TEOS) to the zirconia precursor before hydrolysis.

All gels were placed in sealed containers and aged for 2 months. They were then dried in open air at room temperature, pulverized, and pressed into pellets 13 mm in diameter and 0.5 mm thick.

Double ASAXS experiments were conducted at Beamline 6.2, Daresbury Laboratory, using a Rapid quadrant detector, a Rapid WAXS detector, and a camera length of 3.75 m. Measurements were made in transmission geometry. By aligning the beamline at 17.5 keV, we were able to generate scattering patterns at both the yttrium and zirconium K edges in one experiment by fine tuning the monochromator to six energies around the two absorption edges, which are only 1 keV apart.

Energies were determined by relative positions of the absorption edges from measurements of the X-ray absorption spectra and were chosen such that the energies were −1, −6, and −300 eV from both experimentally determined absorption edges. The resolution of the Si(111) crystal monochromator is $\Delta E/E \sim 10^{-4}$, resulting in an energy resolution of 2.5 eV at 18 keV.[20] Given the energy resolution and the narrowing width of the resonance, it is clear that the data has to be corrected for fluorescence from both edges; see Data Reduction for details.

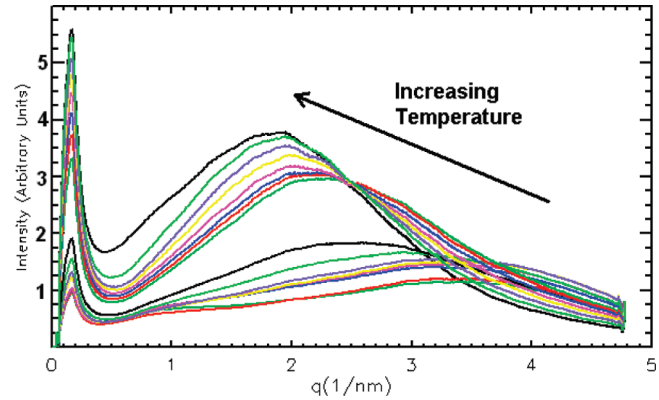

Figure 2. Normal in situ SAXS revealing the growth of a scattering factor "hump" during the sintering of a sol−gel derived yttria-stabilized-zirconia ceramic with 5.6 mol % yttria in air. The feature moves from right to left and increases in intensity as the temperature is increased from 100 to 700 °C. The margin of error in intensity is $\Delta I/I = 2.4 \times 10^{-3}$.

The 0.5 mm thick xerogel pellets were each placed in a furnace with kapton windows so measurements could be made in transmission geometry. All sintering was done in air at atmospheric pressure to assist the combustion of residual organics. Temperatures were slowly increased to 1000 °C with a 10 °C/min ramp up rate. During this period, the six chosen energies (see inset, Figure 4) were cycled at a time resolution of 2 s/frame, giving a time resolution of 20 s per cycle and taking into account motor movements on the beamline monochromator. Further in situ X-ray absorption spectra were taken on the same gels as separate experiments.

Data Reduction

Background measurements were taken from the empty furnace at each energy and subtracted from the scattered sample signal. Data was normalized by measuring the photon counts of the transmitted and reflected beam with two ion chambers during each SAXS measurement. Thus, the scattered signals from only the sample were calculated as eq 10.

$$I_E = \frac{SI_{0S}}{\tau_S t_S} - \frac{BI_{0B}}{\tau_B t_B} \quad (10)$$

Here, S and B are the raw data from the sample inside the furnace and the empty furnace, I_{0S} and I_{0B} represent the intensities of the incident (nonscattered) beams, τ is the transmission measurements, and t is the data acquisition time.

TABLE 1: Sol−Gel Recipes

sol 1 (mL)							sol 2 (mL)	
Zr prop	Y prop	TEOS	acetylacetone	acetic	IPA	mol % Y/Zr	IPA	water
12	0	0	2.25	0.1	6	0	3	2
12	3	0	2.25	0.1	6	2.8	3	2
12	6	0	2.25	0.1	6	5.6	3	2
12	9	0	2.25	0.1	6	8.7	3	2
12	15	0	2.25	0.1	6	14	3	2
12	0	4	2.25	0.1	6	0	3	2
12	3	4	2.25	0.1	6	2.8	3	2
12	6	4	2.25	0.1	6	5.6	3	2
12	9	4	2.25	0.1	6	8.7	3	2
2.21	6	6	0.66	0.01	6	50	3	2

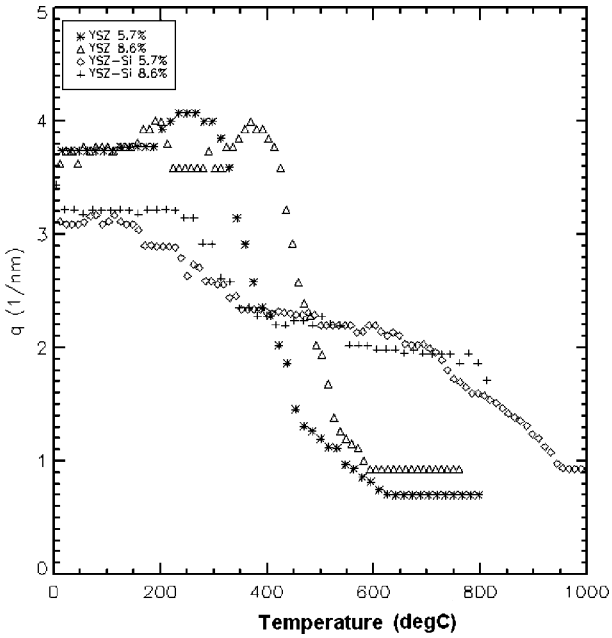

Figure 3. Position of the structure factor maximum on the q scale as a function of temperature (°C). The addition of silica (crosses and diamonds) increases the nucleation temperature, in comparison to straight YSZ (stars and triangles), which nucleates at just below 400 °C. The YSZ and YSZ in silica samples contain 5.7 and 8.6 mol % yttria.

Uncertainties in $I(q)$ were calculated by measuring the amplitude of the noise in the SAXS patterns to give a ratio $\Delta I/I$. Similar calculations were performed to obtain a margin of error in the determined ASAXS normal and resonant terms.

The beamline monochromator was calibrated by measuring the absorption spectra of yttrium and zirconium foils as a function of energy, thus enabling us to pinpoint the true energy of the incident beam. This procedure was repeated before the commencement of each experiment.

Fluorescence and resonant Raman scattering (RRS) are subtracted by taking the high-angle patterns of the wide-angle (WAXS) signal and averaging the photon counts to obtain a single value. These numbers are then normalized against the value obtained from the measurement taken below both edges, where it is assumed the fluorescence and RRS contributions are zero. As fluorescence and RRS are assumed to be uniform over all angles, the numbers are actually the gradient of a function of the form $y = mx$ due to the quadrant shape of the detector. The result of eq 10 is divided by the function thus obtained.

Results and Discussion

In Situ SAXS. Small-angle X-ray scattering reveals the growth of a scattering factor maximum (hump). The feature itself moves to lower values of q as the temperature is increased (Figure 2). Comparing this motion in Figure 3 shows it to be a general case for all the samples. The addition of TEOS to create a silica matrix slows the hump growth, which only becomes more apparent once temperatures are above 780 °C.

Varying yttria content is not a contributing factor to altering the nucleation temperature. This naturally leads to the assumption that zirconia itself is crystallizing independent of yttria in the early stages.

The scattering factor maximum is attributed to the nucleation and growth of nanosized tetragonal and cubic YSZ crystals, as has already been described in similar systems.[13,21,22] These

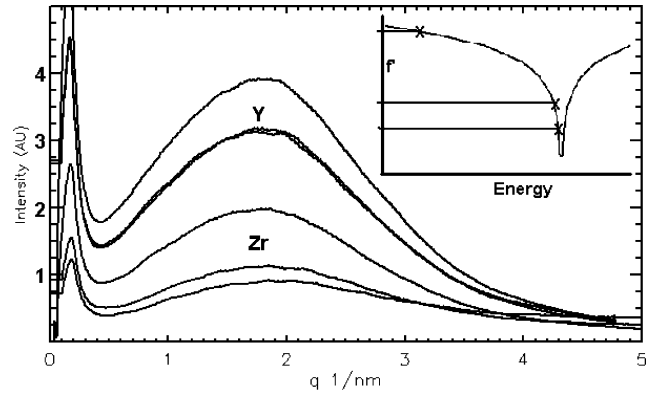

Figure 4. Scattering patterns at six energies: three near the yttrium K edge and three near the zirconium K edge. Shown here are the scattering functions for YSZ in a silica matrix, heated to 900 °C. The anomalous effects are seen as a decrease in overall intensity, as first the yttria and then the zirconia absorb the X-ray beam, and a broadening of the scattering factor maximum close to the zirconium edge. The inset schematic shows the relative positions of the chosen X-ray energies around an absorption edge, with two being within the minimum (−3 and −8 eV) with one far below the edge (−300 eV). This method is followed for both the yttrium and zirconium edges. ($\Delta I/I = 2.4 \times 10^{-3}$.) (Fluorescence and resonant raman scattering contributions are subtracted using large angle WAXS measurements.)

crystals swell rapidly, until the individual sizes are outside of the q window. The initial hump seen in all samples near $q = 4$ nm^{-1} is probably caused by pores in the compressed xerogel that slowly shrink due to the combustion of organic matter in air. Scattering functions of pure YSZ samples show a rapid growth of the maximum after 380 °C. For those in the presence of a silica matrix, crystal growth is gradual; this growth rate increases when temperatures are above 780 °C.

Anomalous (Energy-Dependent) Effects. Small-angle X-ray scattering itself is not enough to determine the initial kinetics of this reaction, as we cannot determine the individual roles of the zirconium and yttrium ions.

The results in Figure 4 show the anomalous effects observed for a sol−gel derived YSZ ceramic at a temperature above the nucleation point and reveal a decrease in intensity and broadening of the maximum as energies approach the zirconia K edge for a given, fixed temperature.

Taking the Porod slopes of the log−log plots (the exponent α) reveals noticeable changes for energies below the zirconium edge, as well as a difference in gradient between those energies on or close to the edge, compared with those below.

Figure 5 reveals a rise in gradient from −4 at the time of nucleation, to between −3.2 and −1.8 for energies at or below the yttrium edge, while results taken from the between-edge energy and those on the zirconium edge reveal shallower gradients. Those on the zirconium edge, in particular, have a Porod exponent close to zero at the highest temperatures. This is due to X-ray absorption by the dense YSZ crystals, leaving the non-YSZ background as the larger contribution. Below nucleation, the Porod scheme does not apply as the samples are still homogeneous xerogels, as opposed to nanoscale particles.

By comparison, YSZ in a silica matrix (Figure 6) shows a steady gradient of around −4 for each energy until nucleation is about to occur. During this period, gradients below the zirconium edge increase in values of between −3 and −2, shown by the step between 700 and 800 °C in the graphs. Energies on the zirconium edge again show Porod exponents closer to zero, though in this case, the convergences are −0.8 and −0.3 for −3 and −8 eV from the zirconium edge, respectively.

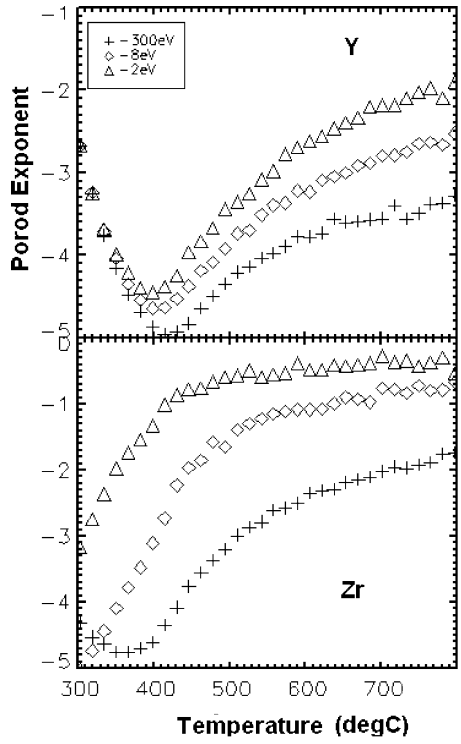

Figure 5. Changes in the Porod exponent of scattering patterns around the Y (top) and Zr (bottom) edges during the sintering of YSZ without silica. The nucleation point is clearly visible for energies below the zirconium edge. In each case, the triangles represent the energy 300 eV below the edge, with the diamonds and crosses being −8 and −3 eV, respectively. Porod exponents from energies on the zirconium edge display gradients close to zero.

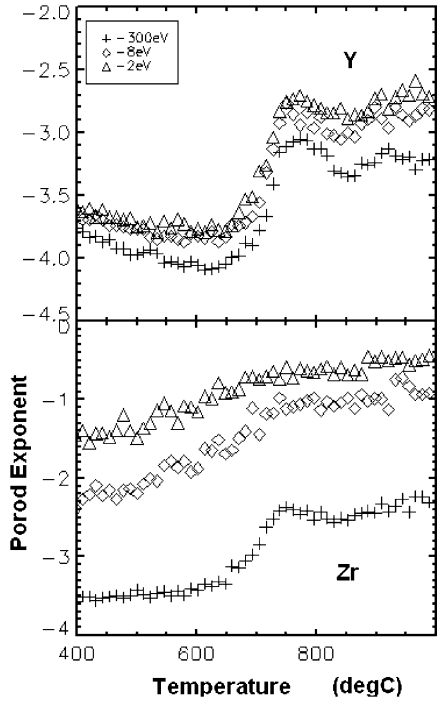

Figure 6. Changes in the Porod gradient of scattering patterns around the Y (top) and Zr (bottom) edges for YSZ in a silica matrix. The nucleation point is much higher than in YSZ without silica (cf. Figure 5), visible as a step in the energies below the zirconium edge. The relative edge positions are the same as in Figure 5.

In both cases, the differences in gradient with increasing energy can be explained by the polydisperse nature of the growing particles. While a gradient of −4 is attributed to a smooth surface, a decrease implies the surfaces are getting rougher with increasing temperature and particle size. The two highest energies, where both yttria and zirconia are highly absorbing, show the Porod background. For straight YSZ, this is air, while for YSZ in silica, the main contribution is the matrix.

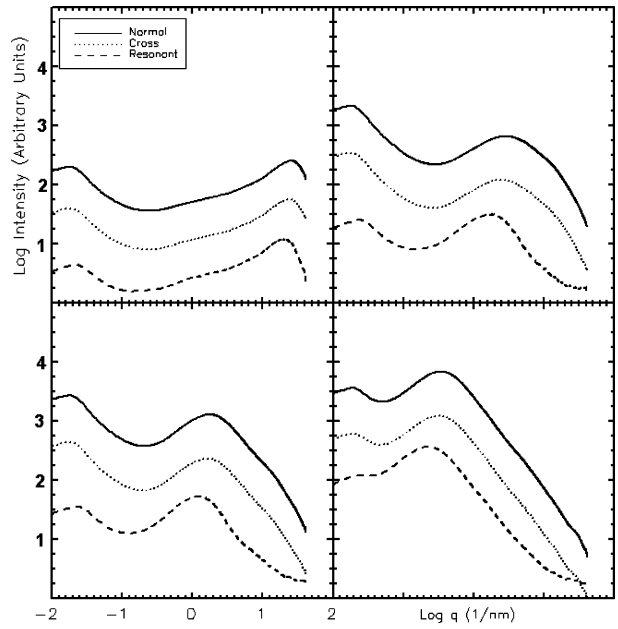

Figure 7. In situ ASAXS scattering patterns (log intensity vs log q) showing the separated normal (continuous line), cross (dotted), and resonant (dashed) scattering contributions. Top left, starting xerogel at room temperature; top right, −380 °C; bottom left, −420 °C; bottom right, −600 °C. The resonant term shows a narrowing during sintering at the intermediate temperatures. At 600 °C, the resonant term becomes identical in shape to the normal term again. ($\Delta I/I$ is 2.5×10^{-3} for the normal and 10^{-2} for the resonant.)

In Situ ASAXS. Figure 7 shows how the three terms of the scattering function evolve with temperature during an in situ experiment of the sintering of yttria-stabilized zirconia. In addition to scattering from macroscopic objects at low q, a structure factor maximum grows at higher q and moves to the left as temperature increases. While the feature is visible in all three terms, there is a clear difference in shape between the normal and resonant terms once the temperature reaches 380 °C. As the samples are heated further, the resonant term once again becomes identical to the normal beyond 640 °C.

The cross term, which comes out as negative, has been reversed to compare it with the other scattering patterns. The sign of the cross term is dominated by the sign of f' in eq 5. As can be seen from Figure 1, f' is negative and increases in magnitude (i.e., becomes more negative) as X-ray energies approach the absorption edge; f' remains negative until energies are well above the zirconium edge.

The difference in width between the normal and resonant terms in q space correlates to a distribution in real space. At the nanometer scale, zirconia particles occupy a region of q different from that of yttria in the early stages of nucleation (at 380 °C). Nucleates then grow with further heating, forcing the zirconia clusters to incorporate the yttria primaries, which increases homogeneity. Patterns in which the normal, cross, and resonant terms are identical in shape (though differing in intensity) are an indication of a two-phase mixture of homogeneous YSZ and air at the nanoscale.

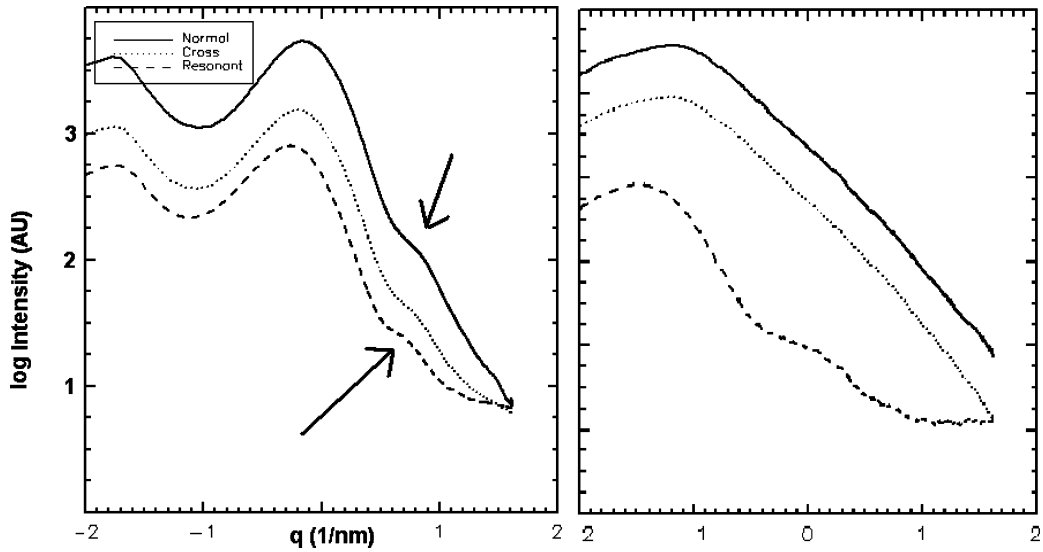

Figure 8. In situ ASAXS scattering patterns (log intensity vs log q) of a YSZ sample with a higher concentration of yttria (Y/Zr = 15 mol %) at 920 °C, showing the separated normal (continuous line), cross (dotted), and resonant (dashed) scattering contributions. Left, YSZ in a silica matrix; right, YSZ without the matrix. Both normal and resonant terms show an additional feature at a larger q in the case of YSZ in a silica matrix, while for a matrix free YSZ, the feature is only resolved in the resonant term. ($\Delta I/I = 2.5 \times 10^{-3}$ for the normal. $\Delta I/I = 10^{-2}$ for the resonant.)

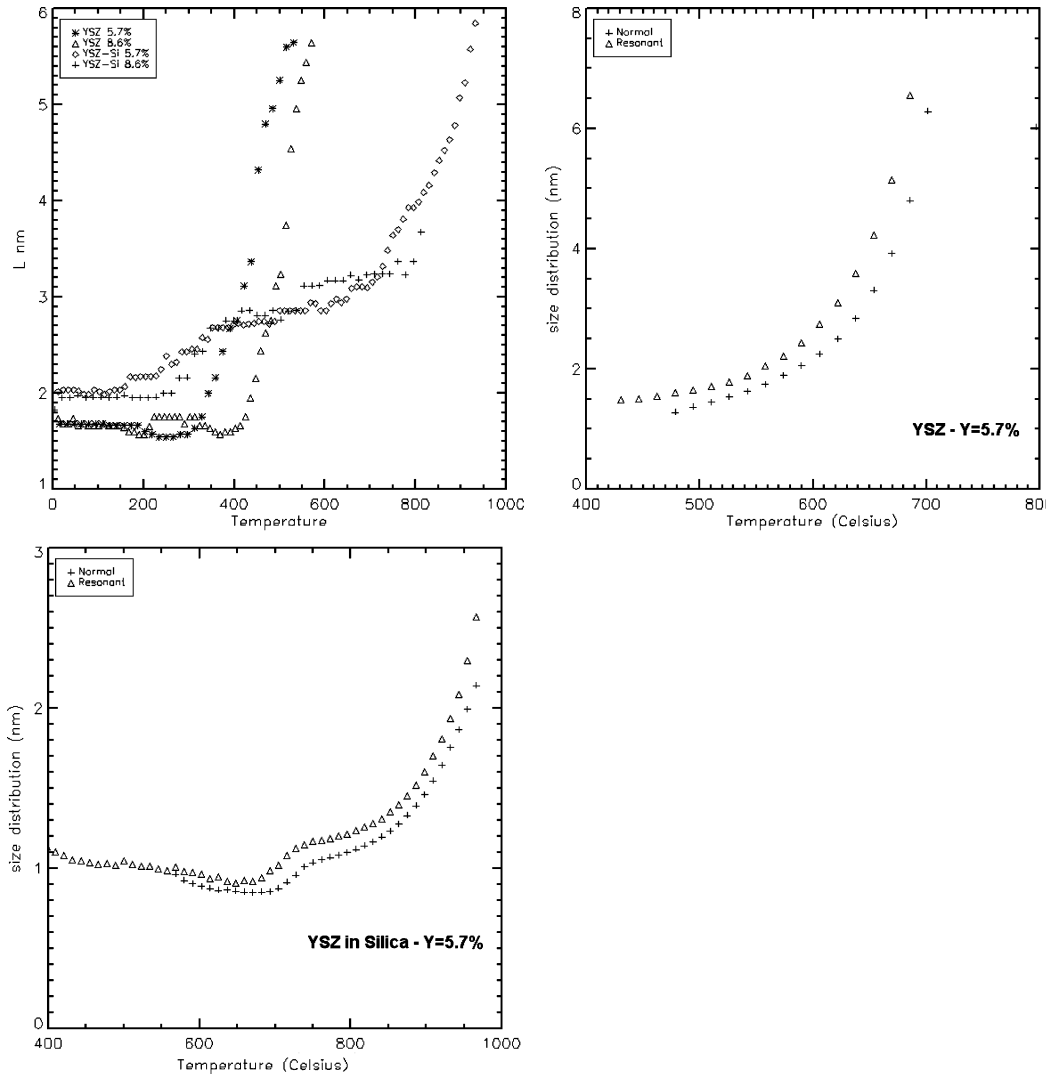

Figure 9. Top left plot shows the correlation length (L) with temperature for YSZ samples with and without a silica matrix. Pure YSZ (stars and triangles) shows a rapid growth just after nucleation. The plot to the top right displays the half width of the structure factor maximum for the normal and resonant terms for YSZ as temperatures are increased. A similar plot (bottom) is shown for YSZ in silica. The presence of a silica matrix narrows the length distribution range to a couple of nanometers at 1000 °C. (Percentages are in terms of mol %.)

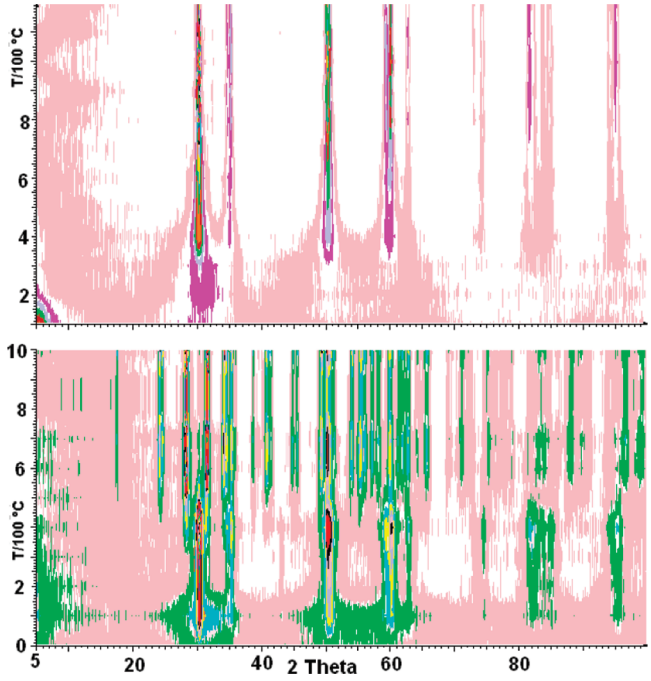

Figure 10. XRD contour maps (count rate vs Bragg angle and temperature). The count rate is color coded. Experiments were conducted ex situ after quenching samples from the temperatures indicated. Top, YSZ (8.7 mol %); bottom, pure (unstabilized) zirconia. The latter exhibits a phase transition on quenching when baking temperatures exceed 500 °C.

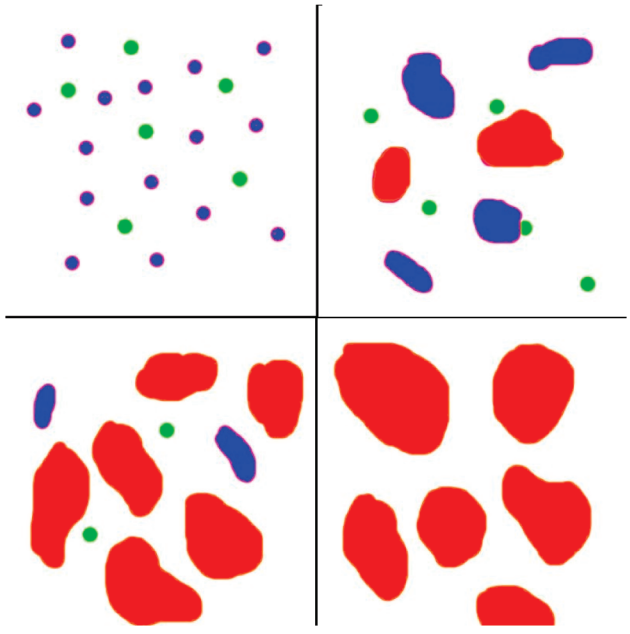

Figure 11. Schematic of the formation of YSZ when heated. In the top left panel, nucleates of zirconia (blue) grow and absorb the yttria (green) as they go along, resulting in an initial mixed-phase state (top right and bottom left). The material becomes single-phase YSZ (red, bottom right) once all the yttria has been incorporated into the growing zirconia crystals.

Additionally, anomalous scattering from high yttria to zirconia ratios indicates the presence of a saturation point, beyond which pockets of surplus yttria will begin to form, which ASAXS is able to resolve in the resonant term (Figure 8, left). In the presence of TEOS, yttria will react with the silica matrix at temperatures over 900 °C to form silicates. This effect is shown in the top half of Figure 8 as a smaller feature to the right of the main scattering factor maximum in both the normal and resonant terms.

Contrasts between the Normal and Resonant Terms: The Role of Yttria and Zirconia. Comparisons of the results have revealed some interesting differences between the normal and resonant terms. Gaussian fitting using Interactive Data Language (IDL) was applied to the scattering factor maxima, and their half widths and position in q space were measured. These values of q were then converted to length scales using the relation in eq 8. The resonant term shows a lower q range and narrowing of the scattering factor maximum, which is described as a larger correlation length. Interestingly, though the maximum is narrower, the resonant half widths reveal a distribution that is wider than that of the normal term. In the cases of YSZ with and without silica, the size distributions diverge with increasing temperature and, hence, can be a measure of an increase in average particle size. These effects can be seen in Figure 9. Results also reveal the presence of silica also decreases the size distribution range for a given correlation length.

$$L = \frac{2\pi}{q} \tag{11}$$

On a subnanometer level, the results are interpreted as further support for the hypothesis that zirconia is playing the dominant role, incorporating yttria into the lattice as the crystals grow. This is a thermally driven reaction where zirconia primary particles drift through the less dense medium (if a silica matrix is present) and coalesce to form nanosized tetragonal crystals. The inclusion of yttria in the growing crystalline structures induces a cubic-phase transition. An increased correlation length and wider distribution with a given temperature in the resonant term can be caused when there are larger pure zirconia crystals. Pure zirconia particles nucleate first, some of which absorb yttria to produce the smaller YSZ particles visible in the normal term. Silica, itself densifying with increasing temperature, slows the thermally driven motion of the zirconia primaries, resulting in smaller crystals and lower size distributions for a given temperature.

In addition to in situ ASAXS, ex-situ experiments were performed on the same samples using X-ray diffraction (XRD) in the materials laboratory at Aberystwyth University. Samples were heated in a furnace in 50 °C steps, and X-ray diffraction was carried out once the sample had cooled to room temperature. Bragg peak formation does not commence until sintering temperatures reach 400 °C for pure YSZ (Figure 10 top). For pure zirconia, quenching reveals a tetragonal−monoclinic-phase transition when the original baking temperatures exceed 500 °C (Figure 10 bottom). Particle sizes were estimated by measuring the half widths of the growing Bragg peaks and by applying the Scherrer equation. Results of this investigation were found to compare to the results obtained from ASAXS.

Figure 11 is a schematic of the formation of sol−gel derived YSZ based upon the results of the experiments. Initially, there is a homogeneous distribution of yttria and zirconia primaries in the xerogel. Upon heating, the zirconia will crystallize, incorporating the yttrium ions as the crystals grow. This induces an initial inhomogeneity which becomes apparent by changes in the resonant term on zirconium ASAXS. The final result is pure cubic-phased yttria-stabilized zirconia in a homogeneous distribution, shown in ASAXS by the three scattering functions identical in shape but differing in intensity.

Conclusion

YSZ and YSZ in a silica matrix have been successfully prepared by the sol−gel method, and the roles yttrium and

zirconium ions play during sintering have been investigated using in situ double ASAXS over two adjacent absorption edges. The presence of a silica matrix increases the crystal nucleation point from 380 to 780 °C. SAXS plots reveal the thermally driven growth of cubic-phased nanocrystals averaging 10 nm in size, which is shown by the presence of a scattering factor maximum. The particle sizes determined from SAXS correlate with those obtained from XRD.

Accurate determination of the atomic scattering factors using X-ray absorption spectra is important to make sure the correct solutions for the normal, cross, and resonant terms are obtained. The resonant term in zirconium ASAXS displays a narrowing of the scattering factor maximum, as well as a peak position at lower values of q, and, hence, a larger particle size. This is interpreted as being due to zirconia playing the dominant role during nucleation. Pure zirconia crystals initially nucleate and absorb yttria as they grow, which results in stabilization of the cubic phase. Contrast between the normal and resonant terms vanishes as the temperature increases and all the yttria is absorbed into YSZ, which makes the sample homogeneous. Yttrium ASAXS shows no observable difference between the normal, cross, and resonant terms for typical YSZ where the yttrium concentration is much lower than that of zirconia.

Further work will be devoted to samples with higher concentrations of yttria, as well as the additional formation of yttrium silicate in the presence of a silica matrix. Other production techniques will also be investigated with ASAXS, such as coated nanoparticles and conventional solid-state reactions.

Acknowledgment. This work was supported by a grant from the U.K. Engineering and Physical Sciences Research Council with support from Diamond Light Source Ltd. Beamtime at Daresbury was awarded by the Science and Technology Facilities Council. We also acknowledge the support of the Higher Education Funding Council for Wales through the Centre for Advanced Functional Materials and Devices.

References and Notes

(1) Subbarao, E. C.; Maiti, H. S. *Solid State Ionics* **1984**, *11* (4), 317–338.

(2) Chervin, C. N.; Clapsaddle, B. J.; Chiu, H. W.; Gash, A. E.; Satcher, J. H.; Kauzlarich, S. M. *Chem. Mater.* **2005**, *17* (13), 3345–3351.

(3) Wang, X. R.; Wang, O. Y.; Gu, J. H.; Tan, W. L.; Jiang, X. Y.; Wy, Z. Y. *Eur. J. Solid State Inorg. Chem.* **1991**, *28*, 605–609.

(4) Dansfielg, G. P.; Fothergile, K. A. *Euroceramics* **1989**, *1*, 275.

(5) Combemale, L.; Caboche, G.; Stuerga, D.; Chaumont, D. *Mater. Res. Bull.* **2005**, *40*, 529–536.

(6) Brinker, C. J.; Scherer, G. W. *Sol-Gel Science, The Physics and Chemistry of Sol-Gel Processing*; Academic Press: New York, NY, 1990; pp 2−11.

(7) Kessler, G. V.; Spijksma, G. I.; Seisenbaeva, G. A.; Hakansson, S.; Blank, D. H. A.; Bouwmeester, H. J. M. *J. Sol−Gel Sci. Technol.* **2006**, *40*, 163–179.

(8) Brinker, C. J.; Scherer, G. W. *Sol-Gel Science, The Physics and Chemistry of Sol-Gel Processing*; Academic Press: New York, NY, 1990; pp 453−509.

(9) Beaucage, G.; Kammler, H. K.; Pratsinis, S. E. *J. Appl. Crystallogr.* **2004**, *39*, 523–535.

(10) Tormal, V.; Peterlik, H.; Bauer, U.; Rupp, W.; Husing, N.; Bernstorff, S.; Steinhart, M.; Goerigk, G.; Shubert, U. *Chem. Mater.* **2005**, *17*, 3146–3153.

(11) Terekhov, A. Y.; Heuser, B. J.; Okuniewski, M. A.; Averback, R. S.; Siefert, S.; Jemian, P. R. *J. Appl. Crystallogr.* **2006**, *39*, 647–651.

(12) Ballauff, M.; Jusufi, A. *Colloid Polym. Sci.* **2006**, *284*, 1303–1311.

(13) Le Messurier, D.; Winter, R.; Martin, C. M. *J. Appl. Crystallogr.* **2006**, *39*, 589–594.

(14) Kirby, N.; Cookson, D.; Buckley, C.; Bovell, E.; St Pierrre, T. *J. Appl. Crystallogr.* **2007**, *40*, p402−p407.

(15) Brumberger, H.; Hagrman, D.; Goodisman, J.; Finkelstein, K. D. *J. Appl. Crystallogr.* **2005**, *38*, 147–151.

(16) Morfin, I.; Ehrburger-Dolle, F.; Grillo, I.; Livet, F.; Bley, F. *J. Synchrotron Radiat.* **2006**, *13*, 445–452.

(17) Goerigk, G.; Haubold, H. G.; Schilling, W. *J. Appl. Crystallogr.* **1997**, *30*, 1041.

(18) Cromer, D. T.; Liberman, D. *J. Chem. Phys.* **1970**, *53*, 1891.

(19) Boyer, D.; Derby, B. *J. Am. Ceram. Soc.* **2003**, *86* (9), 1595–97.

(20) Tang, C. C.; Martin, C. M.; Laundy, D.; Tompson, S. P.; Diakun, G. P.; Cernik, R. J. *Nucl. Instrum. Methods Phys. Res., Sect. B* **2004**, *222*, 659.

(21) Torma, V.; Peterlik, H.; Bauer, U.; Rupp, W.; Husing, N.; Bernstorff, S.; Steinhart, M.; Georigk, G.; Shubert, U. *Chem. Mater.* **2005**, *17*, 3146–3153.

(22) Mroweic-Bailon, J.; Pajak, L.; Jarzebski, A. B.; Lachowski, A. I.; Malinowski, J. J. *J. Non-Cryst. Solids* **1998**, *3* (C8), 385.

JP9012202